Chapter 4

Multiscale structural analysis of polymorphic phase boundaries in doped antiferroelectric Sodium Niobate

4.1 Introduction

Perovskite oxides exhibit various fascinating properties, which makes them useful for several applications, including ferroelectric memory devices, energy storage, sensors and actuators [9, 237, 268, 269, 270]. Currently, lead is a predominant component in functional materials used for various electromechanical applications owing to their high performance [20, 271]. However, environmental concerns trigger the development of functional materials that are environmentally friendly [272]. It is important to note that industrial implementation of the above materials demands high efficiency along with thermal stability.

The functional properties of the perovskite (ABO_3) based materials stem from the displacement of the cations from their centrosymmetric positions at A and B sites, octahedral distortions and/or clockwise/anticlockwise rotation of the BO_6 octahedra

[71, 87, 90, 233, 261]. Typically, off-centred polar cationic displacements and octahedral distortions induced by external stimuli *viz.,* temperature, electric field, etc., enhance the ferroelectric properties, which is a prerequisite for electromechanical applications. On the other hand, octahedral rotations are considered detrimental to the electromechanical response, although they provide excellent thermal stability [118, 119, 273, 274]. Generally, crystalline materials transform from one phase into another through two-phase coexistence under the influence of an external driver, *viz.,* composition, crystallite size, temperature, pressure, electric field, etc. [9, 71, 233]. The width of the phase coexistence region decides the order of the phase transition. In the perovskite-based systems, two conventional phase boundaries have been exploited for various fruitful applications, *viz.,* Polymorphic phase boundary (PPB) and Morphotropic phase boundary (MPB) [9, 29, 275, 276, 277, 278, 279, 280]. The Polymorphic phase boundary is strongly temperature dependent, resulting in a phase transition from one ferroelectric phase to another ferroelectric phase via a very narrow region of phase coexistence. On the other hand, the Morphotropic phase boundary is weakly temperature dependent, and the functional properties of the material become exceptionally high due to coexisting ferroelectric phases (stable for a wide temperature range), making it advantageous for various smart materials applications [30]. The concept of the morphotropic phase boundary and its influence on physical properties (such as ferroelectric and piezoelectric characteristics) has been extensively explored in lead-based ceramic systems *viz.,* $Pb(Ti_xZr_{1-x})O_3$, $Pb(Mg_{1/3}Nb_{2/3})O_3$-$PbTiO_3$, $Pb(Zn_{1/3}Nb_{2/3})O_3$-$PbTiO_3$ etc [56, 111, 281]. The reason behind the high piezoelectricity in lead-based compositions at the morphotropic phase boundary (MPB) is linked to the presence of low-symmetry bridging structures, allowing polarization rotation within a plane [115, 116, 117]. While a strongly temperature-dependent Polymorphic phase boundary and a nearly vertical (weakly temperature-dependent) Morphotropic phase Boundary differ in their temperature responses, similar mechanisms contributing to enhanced piezo-

electric performance have been identified and confirmed for both the phase boundaries [275, 277, 282]. In light of the above discussion, it could be anticipated that a polymorphic phase boundary featuring coexisting ferroelectric phases with octahedral tilts can offer enhanced properties and substantial thermal stability simultaneously.

In chapter 3, we proposed the coexistence of two ferroelectric phases at room temperature in 0.1 $NaNbO_3$- 0.9 $Ba_{0.9}Ca_{0.1}TiO_3$ (hereafter referred to as NN-10BCT) and discussed the possibility of PPB/MPB in the above system [71]. In the current study, we explore the existence of a polymorphic phase boundary in this system, using temperature-dependent synchrotron X-ray diffraction and dielectric data complemented by temperature-dependent Raman analysis and Pair distribution function (PDF) analysis. We find that at ambient conditions, the enhanced dielectric and ferroelectric properties of NN-10BCT are due to the existence of a polymorphic phase boundary, which consists of two distinct ferroelectric phases with space groups $Pmc2_1$ and *Amm2*, respectively. For this PPB, the two-phase coexistence was found over an 80 K temperature range, suggesting significant thermal stability in the vicinity of room temperature. Further, at low temperatures, the system undergoes another phase transition, as suggested by dielectric studies and confirmed via SXRD measurements. The low-temperature phase transition involves the transformation from a single-phase orthorhombic structure (SG: $Pmc2_1$) to a region where two distinct ferroelectric phases coexist *viz.,* orthorhombic (SG: $Pmc2_1$) and rhombohedral (SG: *R3c*). This indicates the presence of another polymorphic phase boundary at low temperatures. Temperature-dependent Raman analysis corroborates the conclusions drawn from SXRD and dielectric studies. However, PDF analysis indicates a relatively stable short-range structure throughout the studied temperature range, contradictory to what has been obtained from SXRD measurements.

4.2 Experimental

Sample with the composition of 0.9 $NaNbO_3$- 0.1 $Ba_{0.9}Ca_{0.1}TiO_3$ has been synthesized using conventional solid-state reaction method. High purity precursor powder of Sodium carbonate(Na_2CO_3), Barium carbonate($BaCO_3$), Calcium carbonate($CaCO_3$), Niobium pentaoxide(Nb_2O_5) and Titanium di-oxide (TiO_2) have been used as starting material. Firstly, all the raw materials were weighted according to composition stoichiometry, followed by Ball milling for 24 Hours in an ethanol medium. After that, the samples were calcined at 1000 °C for 5 hr in an air medium. Afterwards, all the samples were ball-milled and calcined again in similar conditions to rule out the presence of any non-reacted material or unwanted phase. The calcined powder was pressed using a uniaxial hydraulic press, and hence, the formed green pellets were sintered at 1150 °C with a dwell time of 4 hours. The Synchrotron X-ray Diffraction and PDF (Pair Distribution Function) data were collected using Beamline 28-ID-1 (PDF) at NSLS2 (National Synchrotron Light Source) at Brookhaven National Laboratory, with a wavelength of 0.16650 Å. The background-corrected intensity was normalized and reduced to the structure-function S(Q). To obtain the corresponding reduced PDFs, the S(Q) data were then Fourier-transformed using the function

$$G(r) = (2/\pi)\int_{Q_{\min}}^{Q_{\max}} Q[S(Q)-1]\sin(Qr)\,dQ$$

where Q_{max} = 27.8 Å $^{-1}$ and Q_{min} = 0.1 Å $^{-1}$.

Silver electrodes were fired on the top and bottom surfaces of the samples for the subsequent electrical measurement. The dielectric measurements were carried out using a Keysight LCR meter in the temperature range of 100 K - 600 K. The Raman spectra were acquired using a Horiba LabRAM HR Raman spectrometer with an Olympus BX41 microscope attachment. An excitation wavelength of 514.5 nm from a Lexel Model-95 argon ion laser was used. The samples were placed in a Linkam THMS600 microscope

stage for variable temperature Raman measurements. The laser beam was focused onto the sample using a 50x LWD objective (N.A. = 0.50), and the backscattered light was dispersed via a 600 lines/mm grating onto a liquid nitrogen-cooled CCD detector. The data was acquired using LabSpec v5 software. Laser power at the sample was approximately 0.4 mW. This value was checked to verify that no local heating effects from the laser beam occurred.

4.3 Results And Discussion

In the previous chapter, we investigated the composition-dependent structural phase transitions of (1-x) $NaNbO_3$-x $(Ba_{0.9}Ca_{0.1})TiO_3$ (NN-xBCT) for $0.00 \leq x \leq 1.00$ [71]. It has been shown that the AFE phase of pure $NaNbO_3$ transforms into several ferroelectric phases before stabilizing in a paraelectric phase for x=0.25 on substituting BCT. On further increasing the BCT content, the system displays relaxor behaviour up to x=0.90 and, finally, stabilizes in a tetragonal phase with P4mm space group for $(Ba_{0.9}Ca_{0.1})TiO_3$. In the current study, we have examined the technologically significant composition 0.9 $NaNbO_3$-0.1 $(Ba_{0.9}Ca_{0.1})TiO_3$ (NN-10BCT) due to its high dielectric and ferroelectric (i.e., three-fold increment in remanent polarization compared to off-boundary compositions) response [71]. We aim to identify structural phase transitions as a function of temperature and inter-atomic distances, as well as the stability regions of different ferroic phases. The following sections provide a detailed analysis of the dielectric, Synchrotron powder X-ray diffraction patterns, Raman spectroscopy, and Pair distribution function measurements.

4.3.1 Dielectric studies

To investigate the temperature-dependent ferroic phase transitions of the potential composition 0.9 $NaNbO_3$-0.10 $Ba_{0.9}Ca_{0.9}TiO_3$ (NN-10BCT), we have conducted variable

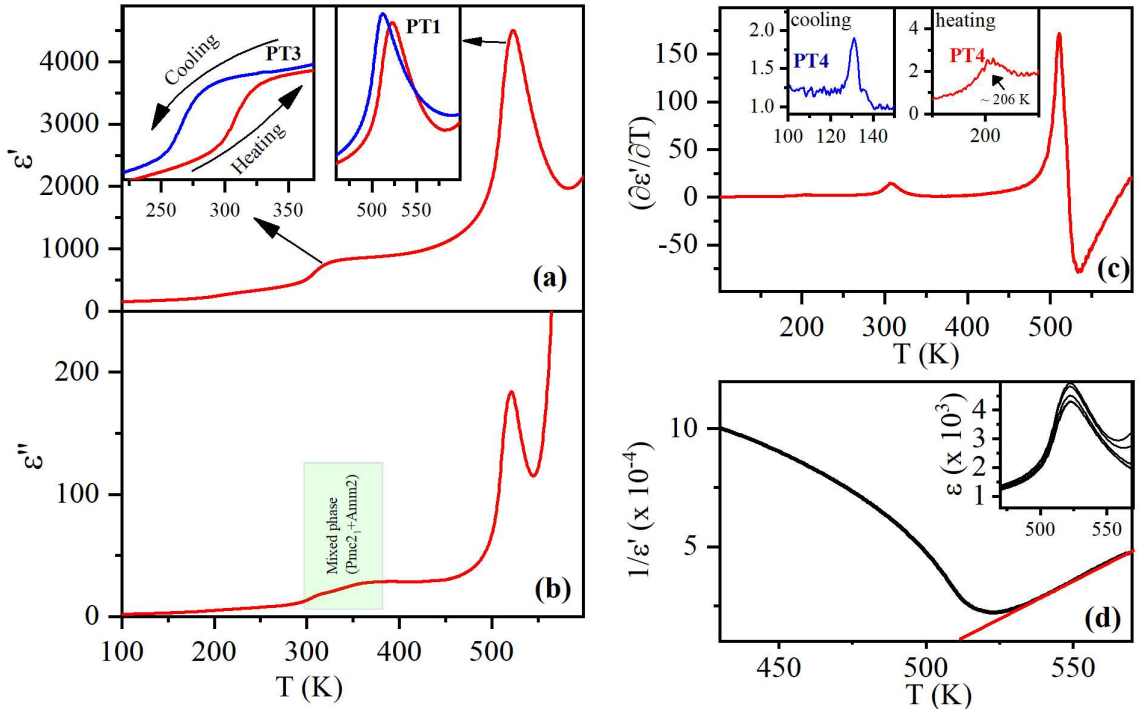

Fig. 4.1 Temperature dependent (a) real and (b) imaginary part of dielectric permittivity in a wide temperature range of 100 K-600 K.(c) Derivative of the real part of dielectric permittivity with respect to temperature marking the weak phase transition around 200 K and 130 K during the heating and cooling cycle respectively. (d) The inverse of dielectric permittivity is plotted against the temperature. The inset shows the frequency-independent dielectric maxima, which is a feature of classical ferroelectric material.

temperature dielectric measurements. The measurements were carried out in heating and cooling cycles within a wide temperature range (100≤T≤600 K). Figures 4.1(a) and 4.1(b) depict the temperature-dependent real and imaginary part of the dielectric permittivity at 10 KHz in the temperature range 100 ≤ T ≤ 600 K. Ferroic phase transitions are typically investigated by identifying anomalies in the temperature-dependent real part of dielectric permittivity $\varepsilon'(T)$. The most pronounced anomaly in temperature-dependent dielectric spectra is associated with the Paraelectric(PE) - Ferroelectric(FE) phase transition. For e.g., in Barium Titanate (BT), this phase transition corresponds to a cubic (PE) to tetragonal (FE) transition observed around 130 [9]. For NN-10BCT, the most profound anomaly in the real part of the dielectric permittivity is observed at 520 K while heating and at 510

K while cooling, indicating a first-order para-ferroelectric phase transition(PT1). Additionally, a prominent anomaly is observed around room temperature, exhibiting significant hysteresis. This suggests a first-order phase transition(PT3) in accordance with the two coexisting ferroelectric phases($Pmc2_1$ & $Amm2$) at ambient conditions reported recently [71]. Notably, this anomaly displays more substantial hysteresis compared to the para-ferro phase transition. In order to observe these phase transitions more clearly, we have plotted the derivative of the real part of the dielectric permittivity with respect to temperature(see Fig. 4.1(c)). This approach helped us in identifying an additional phase transition(PT4) occurring at T ≈200 K during heating and at T ≈130 K during cooling, indicating a large hysteresis of 70 K, suggesting a first-order nature for this phase transition. Figure 4.1(d) presents the inverse of dielectric permittivity as a function of temperature. It demonstrates that the system follows the Curie-Weiss law just above the para-ferro phase transition, a characteristic of long-range ferroelectric systems. Additionally, the dielectric maximum is independent of frequency, which is another feature typical of conventional long-range ferroelectric systems. Detailed synchrotron X-ray diffraction analysis has been conducted to examine stability regions of various ferroic phases and related transition temperatures, which are presented in the subsequent section.

4.3.2 Synchrotron X-ray diffraction Studies

Synchrotron X-ray diffraction(SXRD) measurements were conducted within a wide temperature range of 8 K - 500 K, following a specific protocol. Initially, the sample was cooled to 8 K, and measurements were taken with increasing temperatures up to 500 K. Subsequently, the sample was allowed to cool back, with measurements taken throughout the cooling process. The diffraction patterns have been indexed with respect to a doubled perovskite cell(dpc) ($a \approx 8$ Å). Fig. 4.2 depicts the evolution of SXRD profiles of the main perovskite reflections, i.e., $\{400\}_{\text{dpc}}$, $\{440\}_{\text{dpc}}$, and $\{444\}_{\text{dpc}}$ as well as superlattice

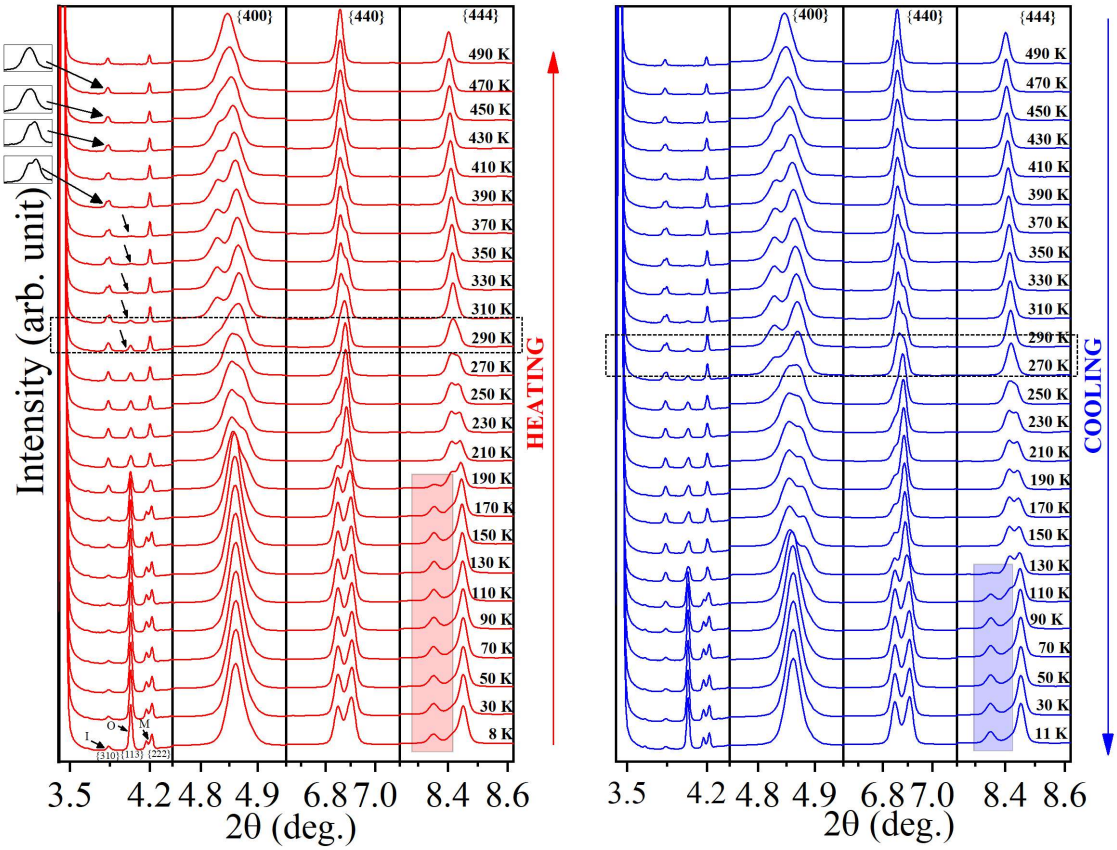

Fig. 4.2 Evolution of Main perovskite reflections *viz.*, $\{400\}_{\text{dpc}}$,$\{440\}_{\text{dpc}}$ and $\{444\}_{\text{dpc}}$ as well as superlattice reflections in (a) Heating (b) Cooling cycle. The shaded rectangle shows the appearance of a new peak beside the $\{444\}_{\text{dpc}}$ reflection around 190 K and 130 K during the heating and cooling cycles, respectively. The dashed rectangle shows the changes in the main perovskite reflections around room temperature.

reflections as a function of temperature for NN-10BCT. The data for heating and cooling cycles have been depicted in the left and right panels of Fig. 4.2, respectively. Although data were collected in 10 K steps, we present the diffraction patterns in 20 K increments for clarity. The reflections present around $3.5° \leq \theta \leq 4.3°$ with odd-odd-odd(marked as O) and odd-odd-even(marked as I) indices are superlattice reflections arising due to out-of-phase and in-phase octahedral rotation, respectively, and are linked with condensation of soft phonon modes *viz.*, $R_4^+(q = 1/2, 1/2, 1/2)$ and $M_3^+(q = 1/2, 1/2, 0)$, respectively [58, 59]. The reflections with all even (eee) type indices are the main perovskite reflections(marked as M). The characteristic main perovskite reflections *viz.*, $\{400\}_{\text{dpc}}$, $\{440\}_{\text{dpc}}$, and $\{444\}_{\text{dpc}}$

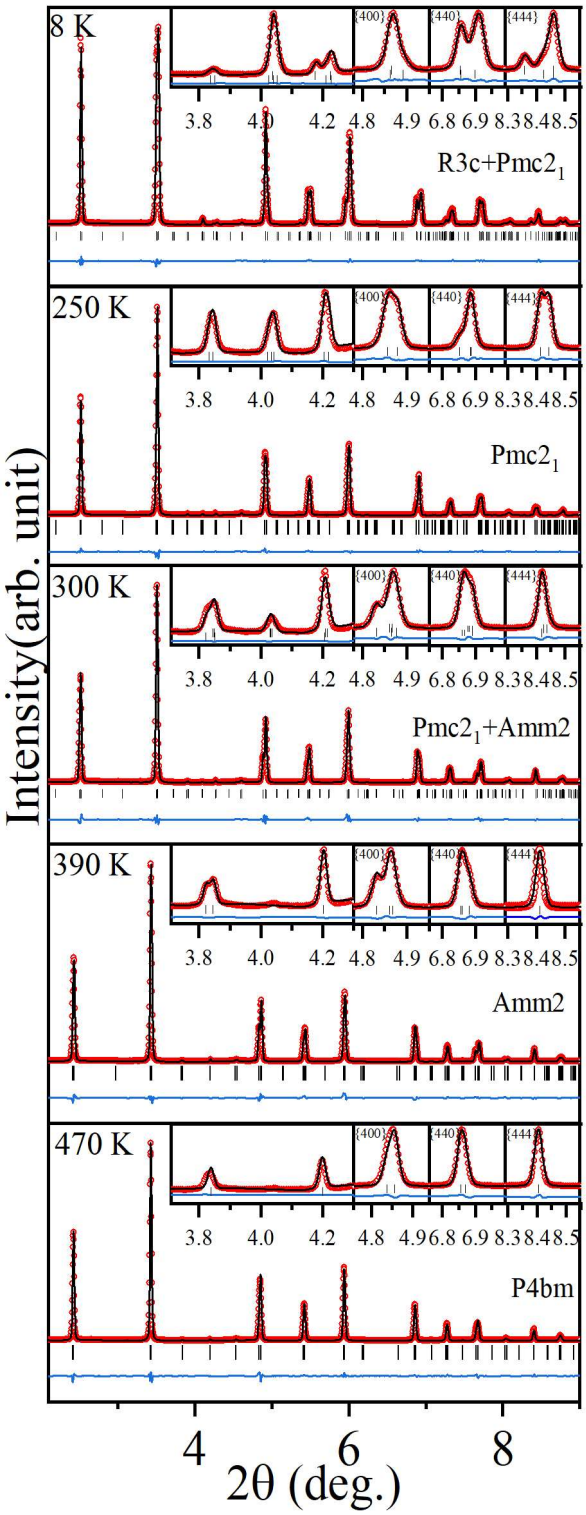

Fig. 4.3 Rietveld refined X-ray diffraction (XRD) patterns of NN-10BCT for a few representative temperatures. The red circles show the observed diffraction data, while the black line shows the simulated pattern. The blue line is the difference between observed and simulated patterns. Inset shows the fitting around the superlattice reflections and main perovskite reflections.

are positioned around 4.7°, 6.9° and 8.4°, respectively. It is important to note that the splitting of the main perovskite reflections corresponds to the distortion observed in the subcell, whereas superlattice reflections result from in-phase, out-of-phase octahedral rotation as well as antiparallel cationic displacements of the A-site cation. Temperature-dependent structural changes can be observed as the splitting of the main perovskite reflection and the appearance/disappearance of the superlattice reflections, shown in Fig. 4.2. The room temperature structure of NN-10BCT consists of two coexisting ferroelectric orthorhombic phases having space group *Amm2* (tilt system: $a_0^+b_0^0c_+^0$, cell size: $a_p \times 2b_p \times 2c_p$) and $Pmc2_1$ (tilt system: $a_+^-a_+^-c_0^+$, cell size: $2a_p \times \sqrt{2}b_p \times \sqrt{2}c_p$) [71]. This two-phase coexistence is confirmed by the presence of unique features corresponding to the two orthorhombic phases, *viz.,* a superlattice reflection linked with out-of-phase octahedral rotation (a unique feature of $Pmc2_1$ phase) and the singlet nature of the $\{444\}_{\text{dpc}}$ reflection (a unique feature of *Amm2* phase). The presence of dielectric anomalies in heating and cooling cycles in the vicinity of room temperature supports the idea of phase coexistence at ambient conditions(shown in the previous section). On increasing the temperature above the room temperature (in the heating cycle), notable changes have been seen in the diffraction profiles. As previously mentioned, the presence of out-of-phase reflection is exclusively attributed to the $Pmc2_1$ (FE2) phase. This unique reflection corresponding to $Pmc2_1$ disappears above 370 K. Consequently, the range for the two-phase coexistence is determined to be 290-370 K, indicating thermal stability of ≈80 K. This temperature-dependent coexistence of ferroelectric phases is known to exhibit high electromechanical properties and is commonly referred to as polymorphic phase boundary(PPB) [29]. When the temperature exceeds 370 K, the system transforms into a single *Amm2* phase, evident by the disappearance of the reflection corresponding to out-of-phase octahedral rotation. The superlattice reflection marked as "I" shows a doublet nature which disappears above 460K, suggesting another phase transition(PT2) from an orthorhombic *Amm2*(FE3) phase to a

Table 4.1 Various models used for fixing the diffraction pattern along with their temperature range in heating and cooling cycles.

Model	Heating	Cooling
R3c+Pmc2$_1$	8K $\leq$ T $\leq$ 200 K	11 K $\leq$ T $\leq$ 130 K
Pmc2$_1$	210 K $\leq$ T $\leq$ 280 K	140 K $\leq$ T $\leq$ 260
Pmc2$_1$+Amm2	290 K $\leq$ T $\leq$ 370 K	270 K $\leq$ T $\leq$ 350
Amm2	380 K $\leq$ T $\leq$ 460 K	360 K $\leq$ T $\leq$ 450 K
P4bm	470 K and above	T > 450 K

tetragonal *P4bm*(FE4) phase(tilt system: $a_0^0a_0^0c_+^+$, cell size: $\sqrt{2}a_p \times \sqrt{2}a_p \times c_p$) . Further, at low temperatures, another phase transition takes place at 200 K during heating and at 130 K in the cooling cycle (see shaded rectangle in Fig. 4.2). This transition is characterized by the emergence of an additional reflection adjacent to the $\{444\}_{\text{dpc}}$ reflection(at 2θ $\approx$8.35, an abrupt increase in the intensity of superlattice reflection corresponding to the out-of-phase octahedral rotation followed by a drastic change in the peak shape/intensity of the $\{400\}_{\text{dpc}}$ reflection.

Table 4.2 Structural parameters, phase fraction, and various agreement factors for NN-10BCT obtained from the Rietveld refinements of the Synchrotron X-ray diffraction pattern at 8 K using two-phase (*R3c+Pmc2$_1$*) coexistence model.

	Space group: *R3c*				Space group: Pmc2$_1$			
Atoms	*x*	*y*	*z*	U_{eq}(Å^2)	*x*	*y*	*z*	U_{eq}(Å^2)
Na1/Ba1/Ca1	0.000	0.000	0.270(2)	0.004(3)	0.000	0.240(15)	0.78(3)	0.015(8)
Na2/Ba2/Ca2	-	-	-	-	0.500	0.247(17)	0.77(3)	0.01(2)
Nb/Ti	0.000	0.000	0.0156(12)	0.0001(8)	0.750(4)	0.7522(17)	0.80(3)	0.0092(17)
O1	0.117(4)	0.343(6)	0.0856(10)	0.002(5)	0.000	0.29(3)	0.31(7)	0.02(5)
O2	-	-	-	-	0.500	0.36(2)	0.33(4)	0.001(11)
O3	-	-	-	-	0.230(16)	0.50(4)	0.072(18)	0.01(3)
O4	-	-	-	-	0.280(14)	0.99(3)	0.513(12)	0.01(3)
	a=5.5224(3) Å, *c*=13.7085(8) Å				*a*=7.8048(9) Å, *b*=5.5348(9) Å, *c*=5.5692(9) Å			
	V= 362.06(3) Å^3, fraction=63.99%				*V*= 240.58(6) Å^3, fraction=36.01%			
Agreement factor: R_{wp}=3.88								

To confirm the evolution of the crystallographic phases as a function of temperature, Rietveld refinements of the SXRD patterns have been carried out using the FULLPROF package [214]. The background was described in terms of linear interpolation between a set of background points of refinable heights. The refined parameters include the zero

Table 4.3 Structural parameters, phase fraction, and various agreement factors for NN-10BCT obtained from the Rietveld refinements of the Synchrotron X-ray diffraction pattern at 250 K using $Pmc2_1$ model.

Space group: $Pmc2_1$				
Atoms	x	y	z	U_{eq}(Å^2)
Na1/Ba1/Ca1	0.000	0.235(8)	0.754(16)	0.004(10)
Na2/Ba2/Ca2	0.500	0.236(9)	0.747(14)	0.016(12)
Ti/Nb	0.750(3)	0.7496(14)	0.763(10)	0.0056(3)
O1	0.000	0.217(13)	0.30(2)	0.01(3)
O2	0.500	0.294(17)	0.30(3)	0.02(3)
O3	0.239(9)	0.541(9)	0.063(8)	0.008(13)
O4	0.270(7)	0.976(12)	0.501(6)	0.012(14)
a=7.8247(4)Å, b=5.5435(3)Å c=5.5725(3) Å				
V=241.71(2)Å^3				
Agreement factor: R_{wp}=3.90				

shift, unit cell parameters, atomic coordinates, thermal parameters, peak shape parameters, etc. For the sake of consistency, we have carried out sequential refinement, i.e. for higher temperatures, we have used refined parameters of lower temperatures as initial parameters. First, we refined the diffraction pattern obtained during the heating cycle of measurements. Based on our previous findings, the room temperature structure was refined using a two-phase model *viz.,* $Pmc2_1$ (O, FE2) + *Amm2* (O, FE3), where O represents the orthorhombic structure, and FE denotes the ferroelectric phase. The same two-phase model was used to refine the diffraction patterns in the temperature range 290 K$\leq$ T $\leq$ 370 K and obtained a very good fit. In the temperature range 380 K$\leq$ T $\leq$ 460 K, a single *Amm2* model could fit the diffraction patterns. Above 460 K, a tetragonal *P4bm* phase was used to fix the diffraction pattern up to the highest measured temperature (i.e. 495 K). Below 290 K, the system completely transforms into a single phase region with $Pmc2_1$ space group, indicated by the disappearance of the shoulder of the $\{400\}_{dpc}$ reflection and the splitting of $\{444\}_{dpc}$ reflection. The single-phase $Pmc2_1$ model very well fits the diffraction patterns with reasonable agreement factors for the temperature range 200 K$\leq$ T $\leq$ 290 K. Another structural phase transition occurs below 200 K, as suggested by the preliminary

Table 4.4 Structural parameters, phase fraction, and various agreement factors for NN-10BCT obtained from the Rietveld refinements of the Synchrotron X-ray diffraction pattern at 300 K using two-phase (*Pmc2$_1$*+*Amm2*) coexistence model.

	Space group: *Pmc2$_1$*				Space group: *Amm2*			
Atoms	*x*	*y*	*z*	U_{eq}(Å^2)	*x*	*y*	*z*	U_{eq}(Å^2)
Na1/Ba1/Ca1	0.000	0.250(4)	0.780(6)	0.010(3)	0.000	0.763(2)	0.000(5)	0.004(4)
Na2/Ba2/Ca2	0.500	0.240(4)	0.760(5)	0.020(4)	-	-	-	-
Nb1/Ti1	0.750(8)	0.752(9)	0.800(5)	0.017(4)	0.500	0.000	0.260(4)	0.004(6)
Nb2/Ti2	-	-	-	-	0.500	0.500	0.260(4)	0.001(6)
O1	0.000	0.220(6)	0.380(7)	0.010(5)	0.000	0.00	0.270(6)	0.001(4)
O2	0.500	0.330(5)	0.350(9)	0.010(1)	0.000	0.500	0.220(5)	0.020(4)
O3	0.240(3)	0.580(3)	0.110(5)	0.013(6)	0.500	0.750(3)	0.250(5)	0.015(4)
O4	0.270(4)	0.970(4)	0.530(2)	0.011(5)	0.500	0.000	0.010(5)	0.010(3)
O5	-	-	-	-	0.500	0.500	0.0046(2)	0.020(2)
	a=7.857(6), *b*=5.556(5) Å, *c*=5.543(3) Å				*a*=3.9207(4) Å, *b*=7.9018(6) Å, *c*=7.8268(7) Å			
	V=241.97(30) Å^3, fraction=31.27%				*V*=242.48(4) Å^3, fraction=68.73%			
	Agreement factor: R_{wp}= 5.49							

analysis of SXRD profiles. The new phase that emerged is likely the rhombohedral *R3c* phase(FE1)(tilt system: $a^-_+a^-_+a^-_+$, cell size: $\sqrt{2}a_p \times \sqrt{2}a_p \times 2\sqrt{3}c_p$ in Hexagonal setting) , a well known low-temperature phase of sodium niobate, or the monoclinic *Cc* (FE5) phase(tilt system: $a^-_+a^-_+c^-_+$, cell size: $\sqrt{6}a_p \times \sqrt{2}b_p \times \sqrt{2}c_p$), which has also been reported for similar compositions at low temperatures [32, 283]. Notably, both of these phases involve only out-of-phase octahedral rotations, making a single-phase model inadequate, as the reflection due to in-phase octahedral tilt remains stable down to the lowest measured temperature(i.e., 8 K). A two-phase model, either *R3c*+*Pmc2$_1$* or *Cc*+*Pmc2$_1$*, is likely to be more appropriate. In order to ascertain the crystal structure of NN-10BCT T < 200 K, we have used the following models to fit the diffraction patterns. In line with the literature considered models include (i) Rhmbhohedral(*R3c*), (ii) Monoclinic(*Cc*), (iii) Orthrhombic (*Pmc2$_1$*), (iv) *R3c* + *Pmc2$_1$*, and (v) *Cc* + *Pmc2$_1$*. Here, the *Cc* and *R3c* phases involve only out-of-phase octahedral rotations, whereas the *Pmc2$_1$* phase includes both in-phase and out-of-phase octahedral rotations. As shown in Fig. 4.2, the in-phase octahedral tilt is visible down to the lowest temperature, ruling out models (i) and (ii) as reasonable options. Additionally, a single-phase *Pmc2$_1$* model is also infeasible, as it does not account for the additional reflection appearing besides $\{444\}_{\text{dpc}}$ reflection. This leaves us with models

Table 4.5 Structural parameters, phase fraction, and various agreement factors for NN-10BCT obtained from the Rietveld refinements of the Synchrotron X-ray diffraction pattern at 390 K using *Amm2* model.

Space group: *Amm2*				
Atoms	x	y	z	U_{eq}(Å^2)
Na/Ba/Ca	0.000	0.7628(18)	0.02(3)	0.008(3)
Ti1/Nb1	0.500	0.000	0.26(3)	0.010(3)
Ti2/Nb2	0.500	0.500	0.26(3)	0.005(3)
O1	0.000	0.000	0.30(4)	0.01(4)
O2	0.000	0.500	0.22(4)	0.01(3)
O3	0.500	0.758(12)	0.28(3)	0.017(13)
O4	0.500	0.000	0.01(4)	0.022(18)
O5	0.500	0.500	0.01(2)	0.023(15)
a=3.9268(3)Å, b=7.8997(4)Å, c=7.8410(5)Å				
V=243.23(3)Å^3				
Agreement factor: R_{wp}=4.74				

(iv) and (v). Ultimately, model (iv) accounts for all the reflections and fits the diffraction patterns very well for the temperature range 8 K$\leq$T $\leq$ 200 K. Therefore, considering the higher symmetry, model (iv) was chosen over model (v). Thus, we have identified another PPB consisting of rhombohedral(*R3c*) and orthorhombic($Pmc2_1$) phases stable over a wide temperature range 8 K $\leq$ T $\leq$ 200 K. Fig. 4.3 shows the refined diffraction patterns at some representative temperatures (see Table 4.2, 4.3, 4.4, and 4.5 for structural models). During the cooling cycle, the same crystallographic models were employed to fit the diffraction patterns, although their temperature ranges differed. The models were selected on the basis of hysteresis (heating/cooling cycles) observed in the dielectric measurements and the peak profile analysis of diffraction patterns. Table 4.1 summarises the various diffraction models used and their corresponding temperature ranges in heating and cooling cycles.

4.3.3 Raman Spectroscopic Analysis

To understand the complex physical behaviour of perovskite-based materials, a technique capable of probing the local structure is also required. Raman spectroscopy is an important

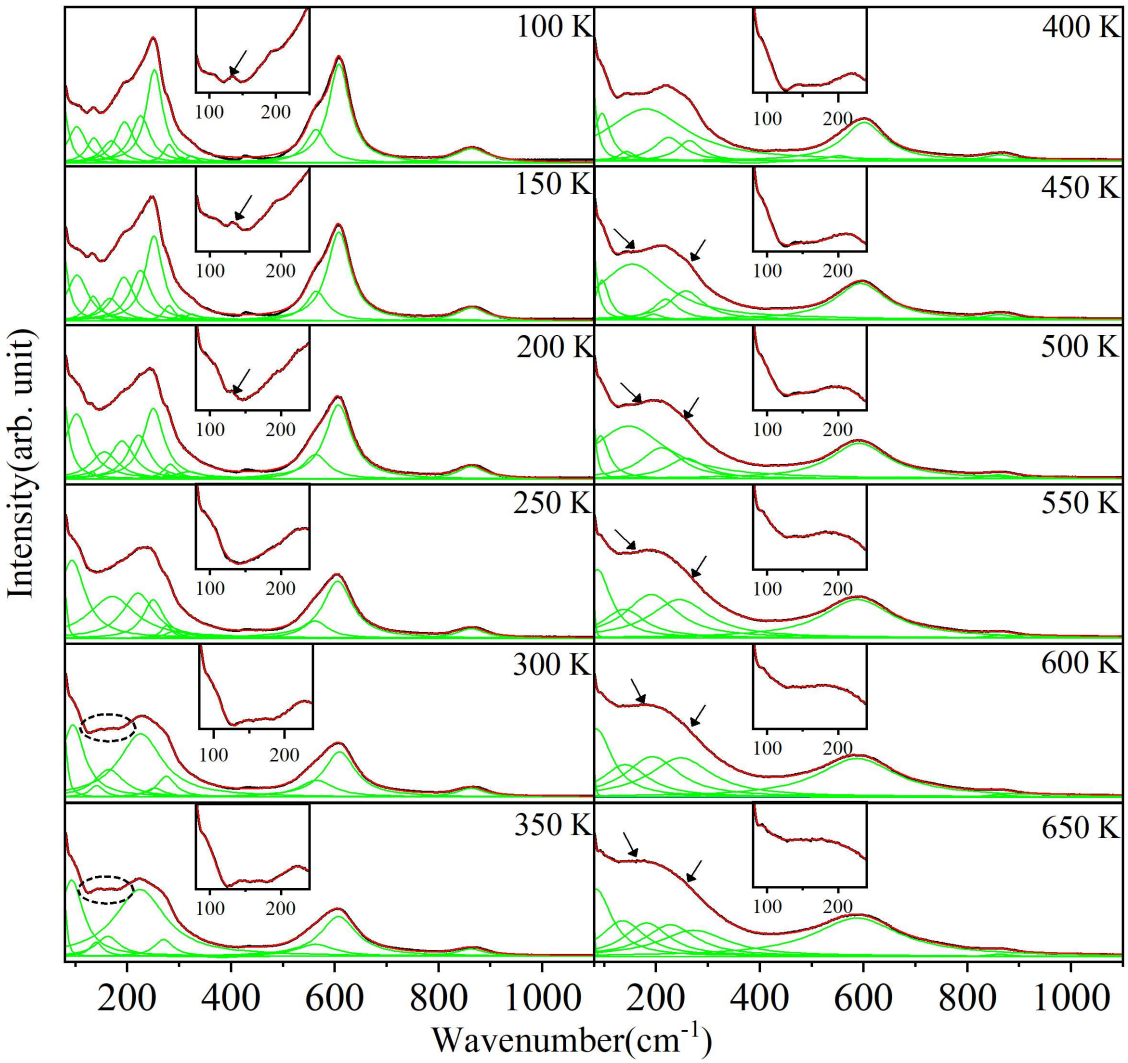

Fig. 4.4 Raman spectra of NN-10BCT at different temperatures in the range of 100-650 K. The Raman spectra have been taken during the heating cycle using the protocol described in the experimental section. All the Raman spectra have been deconvoluted using a suitable number of Lorentz peaks.

Table 4.6 Structural parameters, phase fraction, and various agreement factors for NN-10BCT obtained from the Rietveld refinements of the Synchrotron X-ray diffraction pattern at 470 K using *P4bm* model.

Space group: *P4bm*				
Atoms	*x*	*y*	*z*	U_{eq}(Å^2)
Na/Ba/Ca	0.000	0.000	0.465(3)	0.0124(15)
Ti/Nb	0.000	0.000	0.000	0.0100(3)
O1	0.000	0.000	0.52(1)	0.005(5)
O2	0.2763(17)	0.2237(17)	0.063(4)	0.013(4)
a=b=5.5584(1)Å, c=3.9454(1)Å				
V=121.900(5) Å^3				
Agreement factor: R_{wp}=5.15				

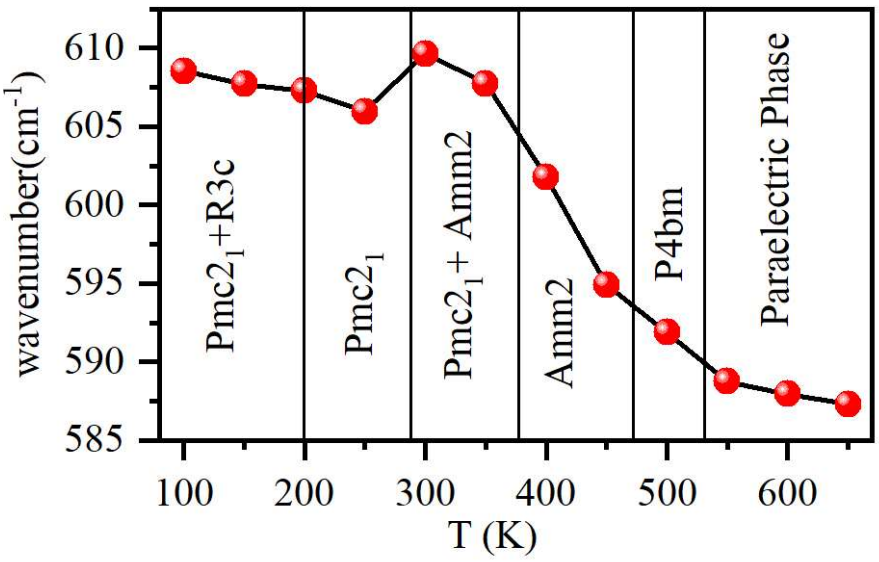

Fig. 4.5 Temperature evolution of the wave number (Raman shift) of stretching Raman mode around 600 cm^{-1}.

tool for this purpose, as it is sensitive to chemical bonding [248, 262, 284]. Moreover, it may provide evidence of structural changes(if any) at intermediate/medium ranges in disordered perovskites, which is usually tracked by the appearance/disappearance of Raman bands as well as changes in the intensities and positions of the Raman bands [285].

The temperature-dependent ($100 \leq T \leq 650$ K) Raman spectra of NN-10BCT are shown in Fig. 4.4. All the Raman spectra were collected during heating mode following the protocol mentioned in the experimental section. The Raman spectra at all the temperatures have been deconvoluted using a suitable number of Lorentz peaks. As can be seen, NN-10BCT exhibits pronounced Raman scattering even at 650 K, although it is in a paraelectric state ($T > T_c$) in which, by symmetry, no Raman-active modes are allowed. The observed Raman bands in the paraelectric state are often attributed to the presence of cationic disorder in the long-range cubic matrix or second-order Raman effect [263, 286]. The Raman spectra of perovskites (ABO_3) primarily results from two factors (i) The motion of A-site cation with respect to BO_6 octahedra (ii) The internal vibrational modes of BO_6 octahedra, such as (a) stretching of B-O bonds and (b) bending of O-B-O bonds. Following this, Raman spectra of perovskite-based materials can be categorised into three main regions based on wavenumbers ($\tilde{\nu}$): (i) $\tilde{\nu} <$ **150 cm^{-1}**: Translational modes of A-site cation with respect to BO_6 octahedra (ii)**150 cm^{-1} $< \tilde{\nu} <$ 450 cm^{-1}**: Bending modes corresponding to O-B-O bonds. (iii) **450 cm^{-1} $< \tilde{\nu} <$ 850 cm^{-1}**: Stretching modes corresponding to B-O bonds [33, 71]. Additionally, some authors attribute the Raman band appearing between 100-150 cm^{-1} to the rotation of BO_6 octahedra [286].

NN-10BCT undergoes a series of antiferrodistortive phase transitions as a function of temperature, and the appearance of the octahedral tilts will affect the bending and stretching Raman modes. The group theoretical analysis was done using the 'SAM' package available at the Bilbao Crystallographic server to calculate the Raman active phonon modes for various phases [253]. Immediately below T_c, the composition NN-10BCT stabilizes into

a ferroelectric tetragonal phase with *P4bm* space group (cell size: $\sqrt{2}a_p \times \sqrt{2}a_p \times c_p$). This tetragonal phase has two molecular units in the primitive cell. Thereby, thirty normal modes are present at the zone centre(calculated by group theoretical analysis) Γ_{Total}= $5A_1 + 3A_2 + B_1 + 3B_2 + 9E$. There are three acoustic modes $\Gamma_{Acoustic}$= $A_1 + E$ and twenty-four Raman active modes Γ_{Raman}= $4A_1 + B_1 + 3B_2 + 8E$. Further, for the ferroelectric orthorhombic phase with space group *Amm2* (cell size: $a_p \times 2b_p \times 2c_p$), there are thirty normal modes at the zone centre: Γ_{Total}= $10A_1 + 2A_2 + 8B_1 + 10B_2$. For this phase, three acoustic modes and twenty-seven Raman modes are theoretically possible *viz.,* $\Gamma_{Acoustic}$= $A_1 + B_1 + B_2$ and Γ_{Raman}= $9A_1 + 2A_2 + 7B_1 + 9B_2$, respectively. Similarly, The ferroelectric orthorhombic $Pmc2_1$ (cell size: $2a_p \times \sqrt{2}b_p \times \sqrt{2}c_p$) phase will have four molecular units in the primitive cell. This results into sixty normal modes at zone centre: Γ_{Total}= $17A_1 + 13A_2 + 13B_1 + 17B_2$ with three acoustic $\Gamma_{Acoustic}$= $A_1 + B_1 + B_2$ and fifty-seven Raman modes Γ_{Raman}= $16A_1 + 13A_2 + 12B_1 + 16B_2$. Finally, for the low-temperature rhombohedral phase with *R3c* space group (cell size: $\sqrt{2}a_p \times \sqrt{2}a_p \times 2\sqrt{3}c_p$) there will be 30 normal modes Γ_{Total}= $5A_1 + 5A_2 + 10E$ out of which there are three acoustic $\Gamma_{Acoustic}$= $A_1 + E$ and twenty-two Raman active modes Γ_{Raman}= $4A_1 + 9E$. Here, A and B are non-degenerate, while E is a doubly degenerate mode. Generally, the number of Raman modes observed experimentally is less than those calculated theoretically (using group theoretical analysis) due to the overlapping of Raman bands [33].

The room temperature(i.e., at 300 K) Raman spectrum for NN-10BCT is similar to what has been reported earlier [71]. Temperature-dependent Raman spectra have been analyzed to track the structural phase transitions in two regions: (i)Region I/Low-temperature region ($100 \leq T \leq 300$ K), (ii)Region II/ High-temperature region ($300 < T \leq 650$ K). In Region I, the Raman spectrum exhibits sharp changes at T >200 K and T≈300 K, indicating two distinct structural phase transitions around these temperatures. The phase transition at T >200 K is marked by the disappearance of a peak around 130 cm^{-1} while the phase

transition at T≈300 K is characterized by the appearance of the broad band around 150 cm^{-1}. The presence of Raman mode around 130 cm^{-1} for T≤200 K is an exclusive feature of the low-temperature phase of sodium niobate (i.e., rhombohedral phase with R3c space group)[161]. In Region II, the characteristic broad band around 150 cm^{-1} disappears gradually for T > 450 K, which may be linked with a structural phase transition above 450 K. It is important to note that these phase transitions are in good agreement with temperature-dependent dielectric and synchrotron X-ray diffraction (SXRD) studies. At high temperatures (T > 550 K), sharp Raman modes disappear, resulting in broad Raman bands, which have been attributed to the disorder(s) present in the high-temperature phases also reported earlier [161].

Although the modifications in the bending modes around the phase transitions are clear, the changes in the stretching modes are less obvious. To monitor the changes in the stretching mode, the Raman shift of the corresponding mode(present at ≈ 600 cm^{-1}) has been plotted against temperature (see Fig. 4.5). A sharp anomaly is observed at T ≈ 300 K consistent with the polymorphic phase transition ($Pmc2_1 \rightarrow Pmc2_1$+$Amm2$) in agreement dielectric and SXRD analysis. Moreover, subtle changes could be noted around other phase transitions *viz.*, $Pmc2_1 \rightarrow Pmc2_1$+$R3c$ and $Amm2 \rightarrow P4bm$. To conclude, the transition temperatures obtained by Raman spectroscopic analysis are found to be consistent with those obtained by SXRD and dielectric analysis.

4.3.4 Pair Distribution Function analysis

The local structures of complex perovskite materials may deviate from their long-range structures ascertained by diffraction experiments. The pair distribution function (PDF), which describes the pairwise correlations among the atoms, is a powerful tool to characterize various aspects of the local structure in disordered perovskites [165, 222, 287, 288]. To better characterize the local structural distortions in NN-10BCT, we undertook pair

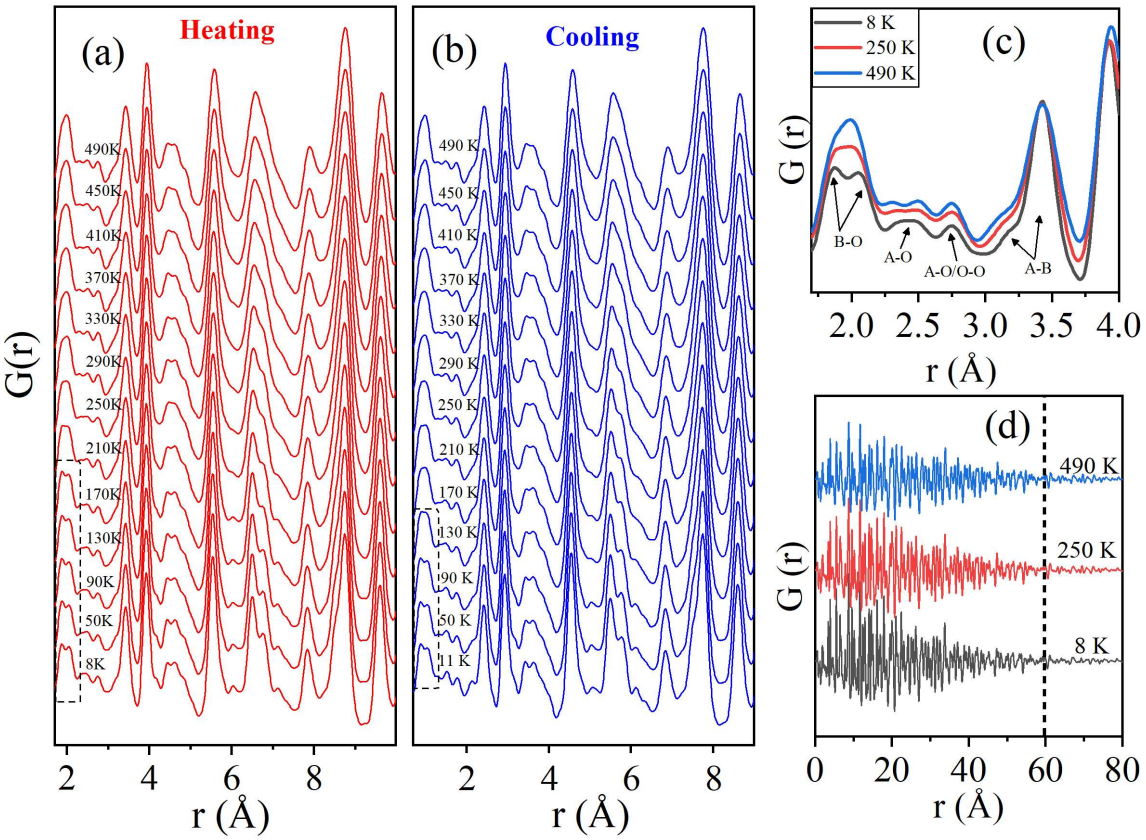

Fig. 4.6 Experimental Variable temperature G(r) for r≈ 1-10 Å for 0.9$NaNbO_3$-0.1$Ba_{0.9}Ca_{0.1}TiO_3$ ceramic powders in (a) Heating (b) Cooling modes, showing the evolution of short-range structures (c) Experimental G(r) within ≈ 4 Å, showing the nearest neighbour pairwise atomic correlations. (d) G(r) depicting the length of structural coherence at some representative temperatures

distribution function analysis of the synchrotron X-ray diffraction data. Fig. 4.6(a) and 4.6 (b) depict the evolution of PDF peak profiles in the heating and cooling modes for a wide temperature range (8 K $\leq$ T $\leq$ 490 K). Fig. 4.6(c) shows the PDF of NN-10BCT for r $\leq$ 4 Å at 8 K, 250 K, and 490 K, respectively, collected during the heating cycle. The arrows have been marked to identify the correlation peak arising from B-O, A-O, O-O, and A-B bonds. At the lowest temperature (i.e., 8 K), there are two distinct sharp peaks for B-O nearest-neighbour correlations at approximately ≈ 1.9 and ≈ 2.1 Å, indicating that Nb is off-centred within the oxygen octahedra [288]. However, as the temperature increases, these two peaks first merge, and then the left peak appears as a shoulder to the

more profound right peak. A broad peak at 8 K around 2.5 Å has been observed, which is attributed to A-O bonds [288]. The broad nature of this peak suggests a distribution of A-O bond lengths. On increasing the temperature, the broad peak primarily splits into two distinct peaks. The peak observed around 2.7 Å could be attributed to both A-O and O-O bonds [288]. Apart from the above-mentioned features, the other peak profile remains almost unchanged, which indicates that the local structure remains relatively stable. Fig. 4.6(d) highlights the termination of G(r), indicating the structural coherence in the material. For quantitative analysis of the structural distortions at short ranges, the PDF patterns were fitted using the program PDFgui [225]. Firstly, we decided to fit the PDF pattern at the lowest temperature, i.e., 8 K, in the region $1.7 \leq r \leq 10$ Å. To start with, we used the two-phase model *R3c+Pmc2$_1$*confirmed from Rietveld refinement of the SXRD data. Although the agreement factor (R_w) was 8.44, some misfits are visible in the PDF fits at low r-regions. The literature on similar disordered perovskites suggests that at short ranges, structures exhibit lower symmetry than the average symmetry obtained from diffraction experiments [219, 289, 290]. Several different local structure models were employed to understand the possible departure of local atomic structure from the long-range structure. We have tried a number of possible models *viz., Pmc2$_1$ + Cc*, *Cc*, *Pm*, etc. These models were derived from numerous studies on similar materials [210, 283, 289]. Among these models, a comparison of the R_w values and the difference curves for the model fit of the X-ray G(r) function indicates that the best fit was achieved with the *Cc + Pmc2$_1$* model (for $1.7 \leq r \leq 10$ Å) similar to what has been reported for NN-BT at low temperatures (see table 4.7 for the description of structural model) [32]. Further, the X-ray PDF is fitted by refining the structural model over successive intervals in real space *viz.,* (i) 1.7-10 Å, (ii) 10-20 Å, (iii) 20-30 Å and (iv) 30-40 Å. Fig 4.7 (a)-(h) shows the comparison of PDF fit and their corresponding R_w parameters for different intervals using the long-range structural model(i.e., *R3c+Pmc2$_1$*) and the most suitable short-range structural model(i.e.,

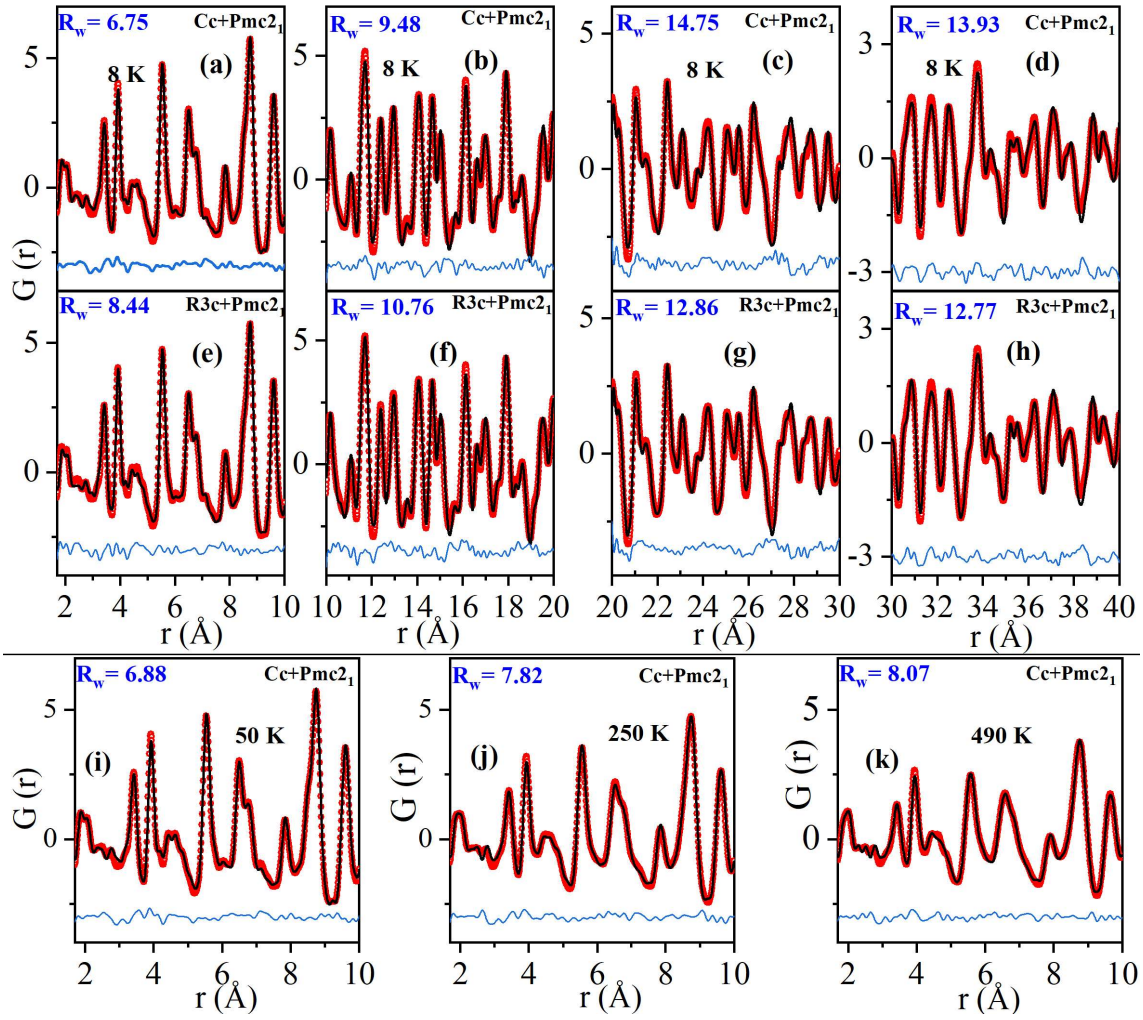

Fig. 4.7 Refinement of PDF profile for different length scale at 8 K using (a)-(d) Cc+Pmc2$_1$ model & (e)-(h) *R3c+Pmc2$_1$* models. PDF refinement with Cc+Pmc2$_1$ model for 1.7$\leq$ r $\leq$ 10 Å at different temperatures *viz.,* 50K, 250 K, and 490 K have been shown in (i), (j), and (k), respectively.

Table 4.7 Structural parameters for PDF analysis performed using a two-phase coexistence model (*Cc* + *Pmc2$_1$*) at 8 K. A similar model was employed to fit PDF profiles at various temperatures. The model used for fitting the PDF profiles with the *R3c* + *Pmc2$_1$* phase coexistence model is similar to the model shown in Table 4.2.

Space group: *Cc*					Space group: *Pmc2$_1$*			
Atoms	*x*	*y*	*z*	U_{eq}(Å^2)	*x*	*y*	*z*	U_{eq}(Å^2)
Na1/Ba1/Ca1	0.000	0.750	0.042(15)	0.0044(9)	0.000	0.257(6)	0.784(36)	0.0033(1)
Na2/Ba2/Ca2	–	–	–	–	0.500	0.285(37)	0.763(43)	0.004(3)
Nb/Ti	0.260(37)	0.248(96)	0.288(77)	0.004(3)	0.748(11)	0.753(17)	0.776(3)	0.0029(3)
O1	0.028(33)	0.251(11)	0.011(72)	0.003(4)	0.000	0.268(67)	0.302(56)	0.0012(3)
O2	0.370(93)	0.511(12)	0.070(15)	0.019(2)	0.500	0.309(10)	0.374(87)	0.0060(8)
O3	0.257(53)	0.012(68)	0.593(87)	0.0020(5)	0.229(25)	0.513(86)	0.105(52)	0.00491(4)
O4	-	-	-	-	0.306(33)	0.971(59)	0.484(6)	0.0100(4)
a=9.383(40) Å, *b*=5.689(33) Å, *c*=5.569(23) Å, β= 123.74(27)					*a*=7.829(7) Å, *b*=5.505(56) Å, *c*=5.597(53) Å			
V= 247.18(77) Å^3, fraction=15.85%					*V*= 241.20(23) Å^3, fraction=84.15%			
Agreement factor: R_w = 6.75								

Cc+*Pmc2$_1$*) concluded after comparing the agreement factors between different plausible models with experimentally observed PDF profiles. Interestingly, as we move towards higher r-regions, the long-range *Pmc2$_1$* + *R3c* model provides better agreement factors. This is evident because, as we move towards higher r values, the model should correspond to the long-range structural model, which is *R3c*+*Pmc2$_1$* in the present case. To explore the temperature-dependent evolution of local structure, we fit the PDF for 1.7 Å $\leq$r$\leq$ 10 Å at different temperatures. Interestingly, the same *Cc* + *Pmc2$_1$* model gives the best fit up to the highest measured temperature, i.e., T = 490 K. In Figures 4.7(i)-4.7(k), we have shown the PDF fits using the *Cc* + *Pmc2$_1$* model at various temperatures. The above discussion results in the following two conclusions: (i) The short-range structure exhibits lower symmetry than that observed at long ranges in powder diffraction data, similar to what has been observed earlier for pure sodium niobate [36]. (ii) At short ranges (1.7 Å $\leq$r$\leq$ 10 Å), the model *Cc* + *Pmc2$_1$* is stable for 8 K < T < 490 K, suggesting that the local structure is thermally stable in comparison to the long-range structure. However, a redistribution of Nb-O bond lengths causes changes around 2 Å in the PDF pattern, which can be fixed using the same model, i.e., *Cc* + *Pmc2$_1$*.

4.3.5 Discussion

Traditionally, phase boundary engineering has been used to enhance the physical response of perovskite-based oxides [291]. The intrinsic mechanism that improves ferroelectric response near the phase boundaries is generally believed to be the flattening of the free-energy profile, a phenomenon commonly associated with most of the structural phase transitions [239, 278, 292]. A flat energy profile provides an easy path for polarization change, as phase boundaries separate two phases with differing polarization orientations. $Pb(Zr_xTi_{1-x})O_3$ is a well-known lead-based solid solution which consists of a Morphotropic phase boundary(MPB) for a nominal composition of x=0.52 [31]. The extraordinary electromechanical properties at MPB could be explained in terms of Gibbs's free energy profiles of the constituting ferroelectric phases [293, 294]. Following the phenomenological theory in the vicinity of MPB, it is theoretically predicted that the energy landscape for polarization becomes quite flat, allowing easy reorientation of polarization in the [111] direction of the rhombohedral (R) phase towards [001] direction of the tetragonal phase on the application of electric field and vice-versa [293, 294]. This results in a transformation from the R phase to the T phase through the intermediate phase(s) with monoclinic symmetry, which was verified experimentally using diffraction techniques [21, 56]. A similar mechanism of property enhancement related to free energy flattening is polarization extension(or contraction) [30].Thus, polarization rotation and polarization extension are very well-known mechanisms observed in the phase boundary region that enhance the properties dependent on the changes in the direction and/or magnitude of polarization. These mechanisms form the foundation of morphotropic and polymorphic phase boundaries [29]. However, PPBs are strongly temperature-dependent in contrast to MPBs (which are weakly temperature-dependent), limiting the use of PPBs in commercial applications [29]. In the present case, we have identified two Polymorphic phase boundaries *viz.,* (i) at ambient conditions consisting of $Pmc2_1$ & *Amm2* phases and (ii) at low temperatures consisting of

$Pmc2_1$ & $R3c$ phases. In literature, a number of Polymorphic phase boundaries (PPBs) have been reported in similar systems, for e.g.:

(i) In $(K_{0.5}Na_{0.5})_{1-x}Li_xNbO_3$, a PPB exists between the orthorhombic and tetragonal phases [275].

(ii) In $Ba(Ti_{1-x}Zr_x)O_3$, two PPBs are observed depending on the composition: one between the orthorhombic and tetragonal phases and another between the rhombohedral and orthorhombic phases [277].

(iii) In Li, Ta, and Sb co-doped $(Na,K)NbO_3$, a PPB is present between the orthorhombic and tetragonal phases [105, 279].

It is important to note that all of the above-mentioned PPBs consist of phases where ferroelectricity arises primarily from cationic displacements and octahedral distortions. Even though octahedral tilting generally hinders ferroelectricity in perovskite-based systems yet it contributes to exceptional thermal stability [118, 119, 273, 274]. In the present system(i.e., NN-10BCT), both the PPBs comprise of phases that have ferroactive cations and octahedral tilt simultaneously. Consequently, the two PPBs are stable in a wide temperature range due to the presence of octahedral tilting. Thus, the thermal stability of these PPBs is comparable to the weakly temperature-dependent MPBs commonly observed in the lead-based systems [236]. Moreover, in addition to the long-range structural complexity, the short-range structure exhibits lower symmetry than the long-range structure, which may also enhance the overall physical properties.

4.4 Conclusions

In this study, we have performed detailed structural phase transition studies on a sodium niobate-based smart system via integrated analysis of temperature-dependent synchrotron

X-ray diffraction, Dielectric, Raman spectroscopic, and Pair distribution function data. Our findings demonstrate the existence of two distinct tilt-oriented and ferroelectrically active PPBs, one stable at ambient conditions and the other at low temperatures. The constituent phases of both the PPBs are distinct and identifiable/separable via Synchrotron X-ray diffraction data analysis. Our findings indicate that the improved ferroelectric response of this material at ambient conditions is due to the presence of a PPB (with two coexisting ferroelectric phases *viz., Amm2* and $Pmc2_1$) stable for a wide temperature range (ΔT $\approx$80 K). Moreover, our analysis suggests the potential of this system for high electromechanical response at cryogenic temperatures due to the presence of another PPB at low temperatures (with two coexisting ferroelectric phases *viz.,* orthorhombic phase with $Pmc2_1$ space group and rhombohedral phase with *R3c* space group) demonstrating phase coexistence for a wider temperature range (ΔT $\approx$190 K in the heating cycle and $\Delta T \approx$120 K in the cooling cycle) in comparison to the PPB observed at ambient conditions. The high thermal stability of the PPBs has been attributed to octahedral tilting (a commonly observed phenomenon in perovskites). This high thermal stability of the PPBs makes them reminiscent of the nearly temperature-insensitive Morphotropic phase boundaries (MPBs). Moreover, Raman spectroscopic analysis strongly supports the conclusions drawn from the synchrotron X-ray diffraction and dielectric analysis. In contrast, PDF analysis reveals the presence of lower symmetries at short ranges (r < 20 Å). However, for the higher spatial regions (r > 20 Å), structural symmetry concluded from PDF analysis is similar to what has been inferred at long ranges (using SXRD analysis). In conclusion, this smart material can serve as a potential candidate for tuning dielectric/piezoelectric/ferroelectric properties with excellent thermal stability at ambient conditions and cryogenic temperatures.

In the next two chapters, we will discuss the compositions with higher BCT content showing relaxor-like characteristics, i.e., NN-25BCT and NN-60BCT.